

Accelerating Low-field MRI: Compressed Sensing and AI for fast noise-robust imaging

Efrat Shimron,^{1,2} Shanshan Shan,^{3,4} James Grover,⁴, Neha Koonjoo,^{5,6}
Sheng Shen,^{5,6} Thomas Boele,^{4,5} Annabel J. Sorby-Adams,^{6,7}
John E. Kirsch,^{5,6} Matthew S. Rosen,^{6,7,8} and David E. J. Waddington^{4*}

¹ Technion - Israel Institute of Technology, Department of Electrical and Computer Engineering and Department of Biomedical Engineering, Haifa, Israel

² Technion - Israel Institute of Technology, May-Blum-Dahl Human MRI Research Center

³ Center for Molecular Imaging and Nuclear Medicine, State Key Laboratory of Radiation Medicine and Protection, School for Radiological and Interdisciplinary Sciences (RAD-X), Soochow University, Suzhou 215123, China

⁴Image X Institute, Sydney School of Health Sciences, Faculty of Medicine and Health, University of Sydney, NSW 2006, Australia

⁵A. A. Martinos Center for Biomedical Imaging, 149 Thirteenth St., Charlestown, MA 02129, USA

⁶Harvard Medical School, 25 Shattuck St., Boston, MA 02115, USA

⁷Department of Neurology and the Center for Genomic Medicine, Massachusetts General Hospital, Boston, MA 02114, USA

⁸Department of Physics, Harvard University, 17 Oxford St., Cambridge, MA 02138, USA

*To whom correspondence should be addressed; E-mail: david.waddington@sydney.edu.au

Portable, low-field Magnetic Resonance Imaging (MRI) scanners are increasingly being deployed in clinical settings. However, critical barriers to their widespread use include low signal-to-noise ratio (SNR), generally low image quality, and long scan duration. As these systems can operate in unusual environments, the level and spectral characteristics of the environmental electromagnetic interference (EMI) noise can change substantially across sites and scans, further reducing image quality. Methods for accelerating acquisition and boosting image quality are of critical importance to enable clinically actionable high-quality imaging in these systems. Despite the role that com-

pressed sensing (CS) and artificial intelligence (AI)-based methods have had in improving image quality for high-field MRI, their adoption for low-field imaging is in its infancy, and it is unclear how robust these methods are in low SNR regimes. Here, we investigate and compare leading CS and AI-based methods for image reconstruction from subsampled data and perform a thorough analysis of their performance across a range of SNR values. We compare classical L1-wavelet CS with leading data-driven and model-driven AI methods. Experiments are performed using publicly available datasets and our own low-field and high-field experimental data. Specifically, we apply an unrolled AI network to low-field MRI, and find it outperforms competing reconstruction methods. We prospectively deploy our undersampling methods to accelerate imaging on a 6.5 mT MRI scanner. This work highlights the potential and pitfalls of advanced reconstruction techniques in low-field MRI, paving the way for broader clinical applications.

Introduction

Low-field Magnetic Resonance Imaging (MRI) is revolutionizing medical imaging by offering cost-effective and portable solutions, yet it faces significant technical challenges. While high-field MRI systems (1.5-3 Tesla) are widely used for their high image quality, low-field MRI systems (0.005-0.1 Tesla) are emerging as a more accessible alternative, particularly in resource-limited settings (1–8). Low-field MRI has already shown promise in diagnosing brain diseases such as stroke and hydrocephalus (9–14), and its demonstrated potential for portable whole-body screening (6, 15, 16) foreshadows a transformation in healthcare, particularly in remote and underserved areas (17).

Nevertheless, the clinical adoption of low-field MRI is hindered by major barriers, primarily its low signal-to-noise ratio (SNR) and, consequently, long scan times. In MRI, the dependence of SNR on magnetic field strength (2, 4, 7, 18, 19) leads to an expected SNR at low field, which is orders of magnitude lower than in clinical MRI. This reduces image clarity and hence limits diagnostic accuracy. To improve SNR, scans are often repeated, and the data are averaged, but this comes at the cost of much longer scan duration, which can, in some cases, exceed one hour (1). Such long scans limit practicality in clinical settings, particularly in critical care, and result in reduced patient comfort and compliance.

MRI scans can be accelerated through data acquisition with a sub-Nyquist rate, a process known as k -space (Fourier domain) undersampling. However, this introduces artifacts that are then removed with image-reconstruction algorithms that infer images from the undersampled data. A vast body of work has been dedicated to developing reconstruction algorithms for high-field MRI (20–23). Specifically, Compressed Sensing (CS) (20, 21) and Artificial Intelligence (AI) (22–24) frameworks have been established as two powerful approaches that enable high-quality reconstructions from undersampled data. CS utilizes prior knowledge about im-

age sparsity in certain transform domains, such as the wavelet domain, while AI methods learn priors directly from the underlying data and the forward encoding model. Both CS and AI approaches have had a transformative impact on high-field MRI (22–24).

Despite their success in high-field MRI, the application of CS and AI remains limited in the low-field MRI domain. CS methods have been explored only in a few studies (25–27), e.g. in the context of Overhauser-enhanced MRI, where SNR is boosted by dynamic nuclear polarization techniques (25), or for the correction of image distortion (27). Meanwhile, AI has primarily been applied to image post-processing tasks such as denoising (28–31), super-resolution (32, 33), image-to-image translation (34–37), and artifact detecting (38), or for reducing the need for electromagnetic interference (EMI) shielding (5, 39). Very recently, a few studies have begun to explore using AI for image reconstruction at low field (40–42). However, the full potential of CS and AI frameworks for accelerating low-field MRI and enhancing its SNR has yet to be fully harnessed.

A key challenge in the development of computational techniques for accelerated low-field MRI is the problem of varying SNR. Modern low-field MRI systems are portable and designed to work in diverse environments, such as motor vehicles (43). While portability offers many benefits, especially in low-to-medium resource regions, it also exposes the device to varying environmental conditions and electromagnetic noise, which can affect the imaging process. The performance of CS and AI methods has been shown to depend on noise variations in high field MRI (44–48) but is relatively unexplored at low field. Hence, while low-field MRI has shown robust, stable performance in controlled lab settings (49), its stability in changing environmental conditions with different noise levels and reconstruction methods requires further analysis.

The optimization of reconstruction methods for accelerated low-field MRI is further hampered by the challenge of evaluating performance. Image reconstruction algorithms are commonly evaluated using quality metrics such as normalized root mean square error (NRMSE) and structural similarity index (SSIM) (50). Those metrics compute the reconstruction quality relative to reference data, e.g. images reconstructed from fully-sampled k -space data. However, in low-field MRI the reference data can be corrupted by substantial noise. Recently, studies in high-field MRI have shown that using unsuitable reference data can lead to biased, overly optimistic results (47, 51). Nevertheless, this critical matter has not been explored yet in the context of low-field imaging, despite the unique challenges of this regime.

Here, we present a comprehensive study that addresses the research gaps in CS and AI reconstruction for accelerated low-field MRI. First, we explore approaches to enable efficient scans while also enhancing image quality. Specifically, we explore different strategies for distributing k -space samples within a fixed scan-time budget and reconstructing images, focusing on strategies combining k -space under-sampling with a variable number of excitations/repetitions (NEX) and CS reconstruction. Second, to further improve image quality and to ensure robustness across the SNR spectrum, we explore and compare methods from three well-established reconstruction frameworks - CS, data-driven AI, and physics-guided unrolled AI methods - and study their performance for varying SNR levels. Next, to raise awareness to critical algorithmic evaluation issues, we conduct the first experiments demonstrating the ‘hidden noise problem’

in low-field MRI. Finally, as illustrated in Figure 1, we evaluate image reconstruction methods using raw high-field data and prospectively undersampled data from an ultra-low-field (6.5 mT) system.

In summary, this work provides the first thorough investigation of MRI reconstruction frameworks across a *broad SNR spectrum* that represents diverse low-field MRI settings. To the best of our knowledge, this aspect of low-field imaging has not been studied before. Specifically, it makes the following key contributions. (1) Exploration of strategies for maximizing speed and image quality within a fixed scan duration. The results show that a strategy combining k -space undersampling, scan repetition (NEX), and iterative reconstruction can outperform fully-sampled acquisitions and provide robustness to varying SNR. (2) A comparative evaluation of canonical MRI reconstruction frameworks for low-field MRI, across a wide SNR spectrum. The results demonstrate that unrolled AI networks consistently outperform CS and data-driven AI, providing both high-quality reconstructions and high stability to SNR variations. They also indicate that CS and data-driven AI exhibit similar performance, yet their relative ranking depends on both the SNR level and acceleration factor. (3) Experimental demonstration of the studied CS and AI frameworks using raw data from both high-field (3 T) and low-field (6.5 mT) scans, including experiments with prospectively undersampled data. (4) The first demonstration of the *hidden-noise problem* in low-field MRI, which shows that computing image quality metrics relative to reference images containing different levels of noise can change the algorithmic ranking. As low-field MRI is characterized by high levels of noise, this demonstration can raise awareness of this important matter.

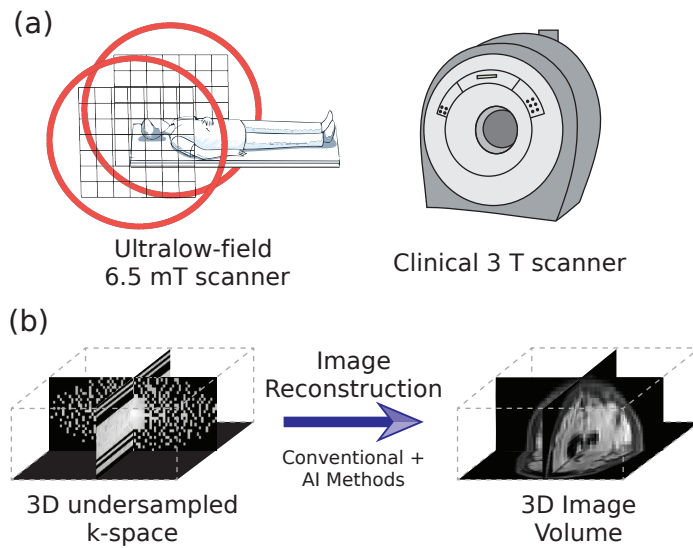


Figure 1: **Reconstruction accuracy across field strengths.** (a) MRI data in this study were collected using an ultra-low field (6.5 mT) MRI scanner based on a biplanar electromagnet (1), and a conventional 3 T MRI scanner, as illustrated schematically. Additional data were sourced from the fastMRI database and synthetically degraded by the addition of Gaussian noise to allow for a wide signal-to-noise ratio regime to be analyzed (52). (b) Raw 3D k -space data were collected via retrospective and prospective acquisitions using a range of sampling patterns. This figure demonstrates a 3D variable-density undersampling pattern. The accuracy of 3D volumes reconstructed from k -space data using conventional methods such as compressed sensing was compared to leading data-driven and model-driven techniques based on neural networks.

Results

Signal averaging and subsampling for efficient acquisitions in low SNR

Data acquisition with low- and especially ultra-low-field MRI systems differs from high-field MRI in that low-field data are commonly acquired with many repetitions per k -space line to improve SNR. We begin by characterizing the potential of undersampling methods to improve image quality without changing the overall scan duration. We explore different approaches to distribute samples within a fixed scan time ‘budget’, by reducing the number of points acquired and increasing the number of averages, denoted by NEX.

Specifically, we compare three sampling strategies (Figure 2a): (1) a fully-sampled acquisition without repetitions (i.e. $NEX = 1$) and inverse fast Fourier transform (IFFT) reconstruction; (2) a $2\times$ accelerated scan ($R = 2$) where data are undersampled using a *solid disc* mask or (3) a *Poisson disc* mask. In cases (2) and (3) the scan is repeated twice ($NEX=2$), resulting in an overall scan time that is identical to the first case, but with the undersampled images reconstructed via CS.

To explore these sampling strategies as a function of SNR, we generated a low-resolution dataset of 100 brain volumes using the fastMRI database (52). Specifically, high-resolution brain volumes acquired at 1.5 T or 3 T were downsampled and transformed to single-coil $64 \times 75 \times 25$ k -space data, to align with the resolution of image data from our 6.5 mT scanner (see Materials and Methods for further details). For each SNR value tested, the k -space data were degraded to the stated SNR through the addition of complex additive white Gaussian noise. The quality of brain volumes reconstructed using different sampling approaches was quantitatively evaluated using normalized root-mean-square error (NRMSE) and structural similarity (SSIM) metrics.

The results (Figure 2b) indicate that for very low SNR values, typical of low-field MRI, CS reconstruction of Poisson-disc undersampled data gives the best image reconstruction metrics (low NRMSE, high SSIM). In fact, an approach combining $2\times$ undersampling, 2 repetitions, and CS reconstruction is superior to a single acquisition and IFFT reconstruction. This improvement at low SNR likely stems from the ~ 3 dB increase in k -space SNR that comes with an additional signal averaging and the denoising effects of CS reconstruction. Conversely, at high SNR values (>30 dB), image quality metrics indicate that the best reconstructions are obtained by acquiring fully-sampled k -space data without repetitions.

We also examined changes to the random undersampling mask, for the same acceleration factor, and found that this has a very limited impact on subsequent reconstruction performance. In Supplementary Figure 1 we repeat this sampling experiment with an $R = 2$ Poisson disc mask that fills the corners of k -space and yields very similar results to those shown in Figure 2. A thorough examination of even more quasi-random undersampling masks in ultra-low field MRI can be found in Reference 53.

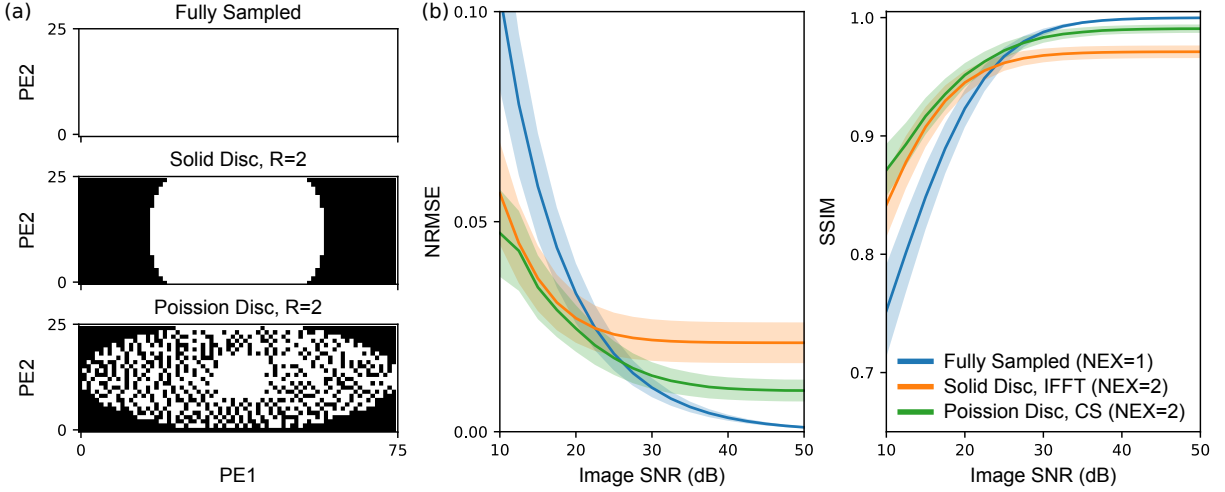


Figure 2: **Comparison of three sampling-reconstruction strategies for utilizing a fixed total scan time ‘budget’, with evaluation across varying SNR values.** (a) Illustration of the three strategies. (1) Acquisition of fully-sampled k -space data without repetitions (NEX = 1) and inverse Fast Fourier Transform (IFFT) reconstruction. (2) Solid disc under-sampling with $R = 2$ and two repetitions (NEX = 2) and compressed sensing (CS) reconstruction. (3) Poission disc undersampling with $R = 2$ and two repetitions (NEX = 2) and CS reconstruction. (b) Evaluation of the three strategies using input data with various SNR levels. Reconstruction quality was measured using the normalized root-mean-square error (NRMSE) and structural similarity index (SSIM) metrics. Solid lines indicate the mean and shaded regions indicate the standard deviation across 100 brain volumes. The x -axis SNR values are calibrated to the Image SNR of the fully-sampled image (i.e. 20 dB is a linear Image SNR of 10, 40 dB is a linear Image SNR of 100). Notably, the results indicate that the combination of $2\times$ Poission Disc undersampling, 2 repetitions and CS reconstruction results in higher reconstruction quality than the other two approaches.

Exploring AI-based reconstruction across the SNR regime

Having established that Poisson disc undersampling can improve image quality when SNR is low, we now turn to examining the comparative advantages of different reconstruction frameworks across the SNR regime. In addition to the IFFT and l_1 -wavelet CS methods described above, we analyze the performance of two well-established AI frameworks: (i) a data-driven framework trained on the forward encoding model known as AUTOMAP (54), and (ii) a physics-guided unrolled neural network (55). Briefly, the AUTOMAP network consists of 2 fully connected layers and 4 convolutional layers that, by supervised learning on the forward encoding, learns to invert the spatial decoding process between k -space and image space without any prior knowledge. The unrolled network incorporates known models of MRI physics models and, in our implementation, consists of 10 iterative blocks, each incorporating a data-fidelity term with forward and backward transforms that reduce image artifacts through convolutional operations.

The networks were trained on a corpus of more than 250,000 brain slices obtained from fastMRI (52) and the Human Connectome Project (56) (see Material and Methods for further details). Experiments were performed with single-coil k -space data sampled using Poisson-disc masks and acceleration factors of $R = 2, 4$. To evaluate the reconstruction quality, the NRMSE and SSIM metrics were calculated across the test set (100 fastMRI brain volumes) (see Figure 3). Corresponding image examples and sampling masks are shown in Figure 4.

The results (Figure 3) indicate that the unrolled network provides the best reconstruction quality for the range of SNR values and acceleration factors analyzed in this study, as quantified by the image quality metrics (low NRMSE, high SSIM). The visual comparison (Figure 4) further demonstrates that the unrolled network provides high-quality reconstructions, as all reconstructed images are free of aliasing artifacts and have clear edges. These results indicate that the unrolled network outperforms the three other methods (IFFT, CS, and AUTOMAP) for both low-field and high-field MRI data.

Furthermore, we also observe that the relative ranking of CS and AUTOMAP is inconsistent; it depends on both the acceleration factor and the SNR level (Figure 3a). For example, for $R = 2$, the quantitative metrics indicate that AUTOMAP outperforms CS reconstruction in the high SNR regime but that when SNR is reduced (< 19 dB), CS performs better. However, the reconstructions of both methods exhibit similar quality, without noticeable aliasing artifacts (Fig. 4a). In contrast, at $R = 4$ (Fig. 4b), both AUTOMAP and CS yield images with aliasing artifacts, which are blurrier than the unrolled network’s reconstruction. While the noise in the AUTOMAP and CS reconstructions is observed to decline at high SNR (40 dB), the aliasing artifacts remain. This is also reflected in the NRMSE and SSIM quality metrics (Fig. 3b). Importantly, at $R = 4$, the standard deviation of NRMSE/SSIM metrics is observed to decrease with the SNR level for the unrolled network but not for CS and AUTOMAP.

In summary, the results indicate that the unrolled network outperforms the other methods and exhibits high robustness to SNR levels, the performance of CS and AUTOMAP is not consistent when the acceleration factor increases from $R = 2$ to $R = 4$, and that *only* the unrolled network can effectively recover fine details for $R = 4$.

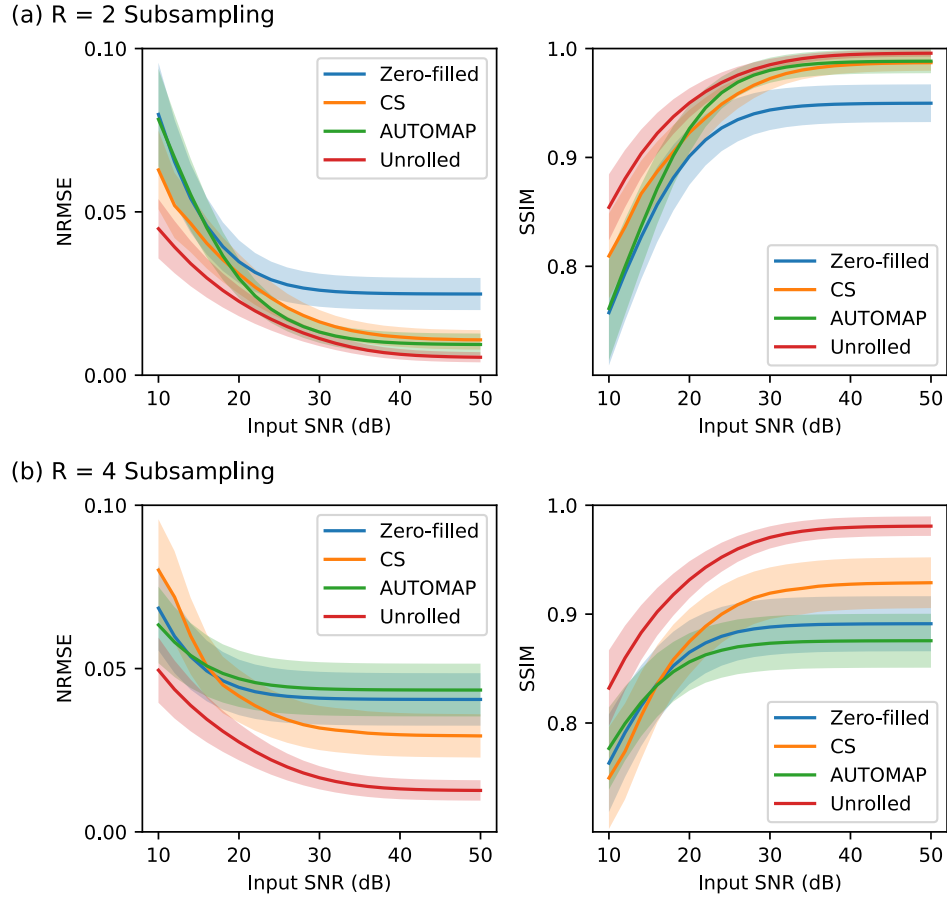


Figure 3: **Quantitative evaluation of reconstruction quality at different signal-to-noise ratios (SNR) levels.** The mean normalized root mean square error (NRMSE) and structural similarity (SSIM) of 100 brain volumes reconstructed from undersampled, low-resolution FastMRI k -space data are shown for acceleration factors (R) of 2 and 4 in **a** and **b**, respectively. The SNR of the input signal (k -space) was adjusted by adding synthetic Gaussian noise scaled to the ground truth k -space data. Four reconstruction methods were compared: zero-filled Inverse Fast Fourier Transform (blue), Compressed Sensing (CS, orange), AUTOMAP (green), and unrolled AI (red) techniques. Shaded regions indicate the standard deviation of the metrics. Note that the unrolled AI outperforms all other methods in all cases (lowest NRMSE, highest SSIM).

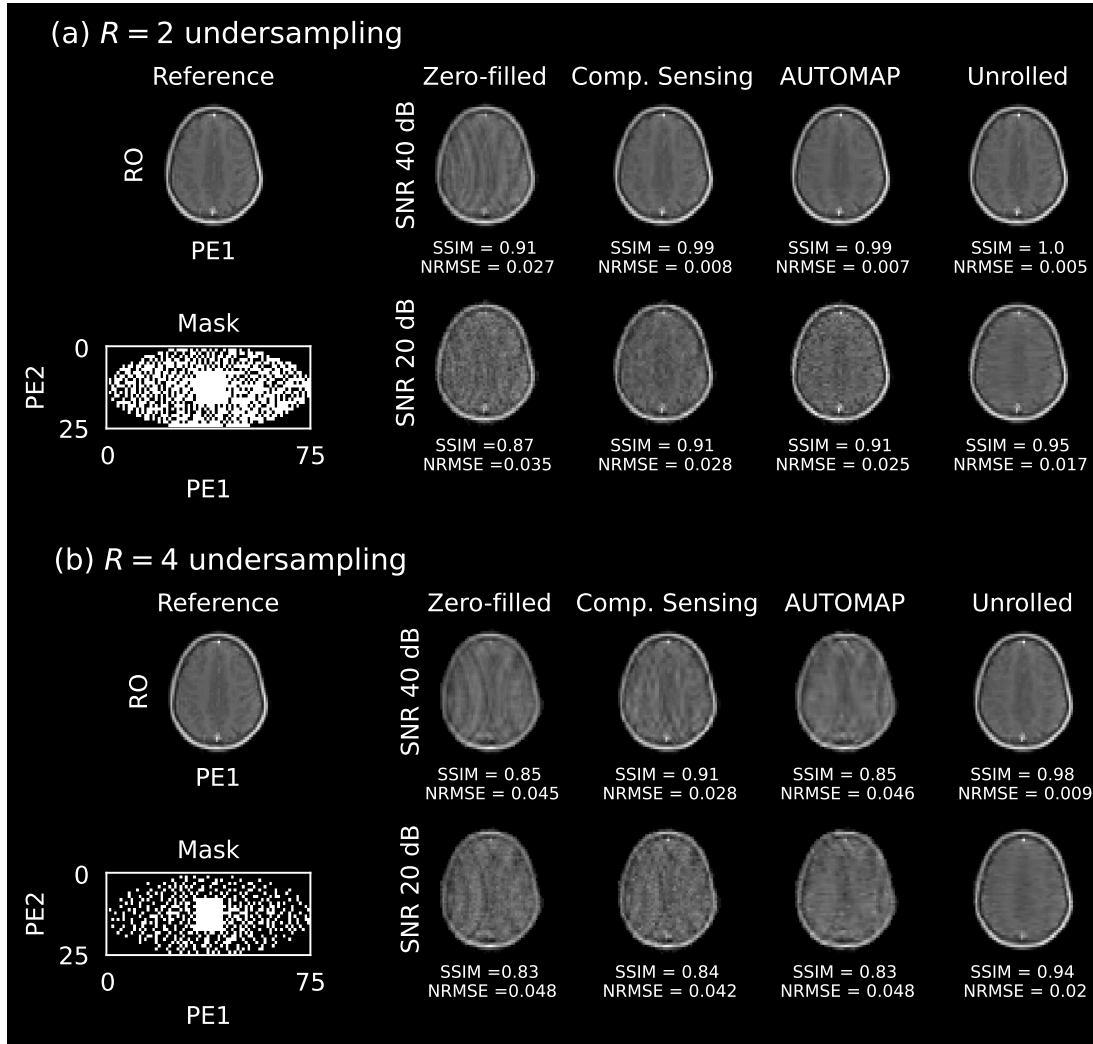


Figure 4: **Visual comparison of reconstruction performance on retrospectively undersampled FastMRI data.** Reconstructions of the central slice from a brain volume are shown for the zero-filled Inverse Fast Fourier Transform, Compressed Sensing, AUTOMAP, and unrolled AI methods, for acceleration factors (R) of 2 and 4 in **a** and **b**, respectively. The Poisson disc masks used for undersampling are also displayed, in a plane consisting of the Phase Encode 1 (PE1) and Phase Encode 2 (PE2) directions. The reconstructions are shown for k -space data with ‘high’ and ‘low’ signal-to-noise ratios (SNR) of 40 dB and 20 dB, respectively, in the PE1 and Readout (RO) plane. Note that for $R = 4$, only the unrolled AI method can remove the undersampling artifacts.

The hidden noise problem in ultra-low field MRI

The quantitative comparisons we have shown thus far have made the implicit assumption that the reference data, which is used for quantifying algorithmic performance, consists of noiseless ‘ground truth’ images. However, in MRI, it is generally infeasible to experimentally measure a noiseless image. Moreover, it is increasingly recognized that even small variations of the reference data will negatively impact the accuracy of error metrics such as NRMSE and SSIM; this was demonstrated for different scenarios in high-field MRI in References 47 and 51 . However, although this ‘hidden noise’ problem is of extra importance in the ultra-low field regime due to very low SNR, it has not yet been explored in this context.

Here we conduct the first study and demonstrate the ‘hidden noise’ impact on error metrics. We scanned a head-shaped phantom at 6.5 mT, as shown in Figure 5. Fully-sampled reference data were acquired with a number of excitations (NEX) of 16 and 256. Next, the NEX = 16 k -space data were retrospectively undersampled ($R = 2$) and used to reconstruct phantom images via conventional and AI-based techniques. SSIM and NRMSE metrics calculated relative to the NEX = 256 reference clearly show the unrolled AI reconstruction as the superior reconstruction method (Figure 5). Structures in the unrolled AI reconstruction also have clear edges and are denoised relative to images produced with alternate reconstruction methods. However, when metrics are recalculated against the NEX = 16 reference image, the best reconstruction appears to have been generated via a Zero-filled IFFT, even though this method violates the Nyquist criterion and contains blurry features. Likely, the high SSIM and low NRMSE of the zero-filled IFFT occur because the same underlying k -space data were used for the undersampled k -space and reference k -space, and there is no denoising in the IFFT operation. Importantly, we note that using the same underlying k -space for reference and undersampled data is common practice in accelerated MRI studies due to the time challenges inherent in collecting a high SNR reference image; our NEX = 256 scan took nearly 2 hours to acquire, a timeframe more amenable to motion-free phantom imaging than humans (57).

The AI networks used in the main body of this paper were trained with mean-square error (MSE) loss. However, it is increasingly recognized that such ‘full reference’ metrics are not the best metric for measuring image quality as perceived by humans (58). Hence, we explored the impact of training the unrolled AI network with a ‘perceptual loss’ based on layer activations in the AlexNet CNN (59). While images reconstructed with a perceptually trained network showed poorer NRMSE and SSIM values, it appears that higher frequency details may be better reconstructed (see Supplementary Figure 2).

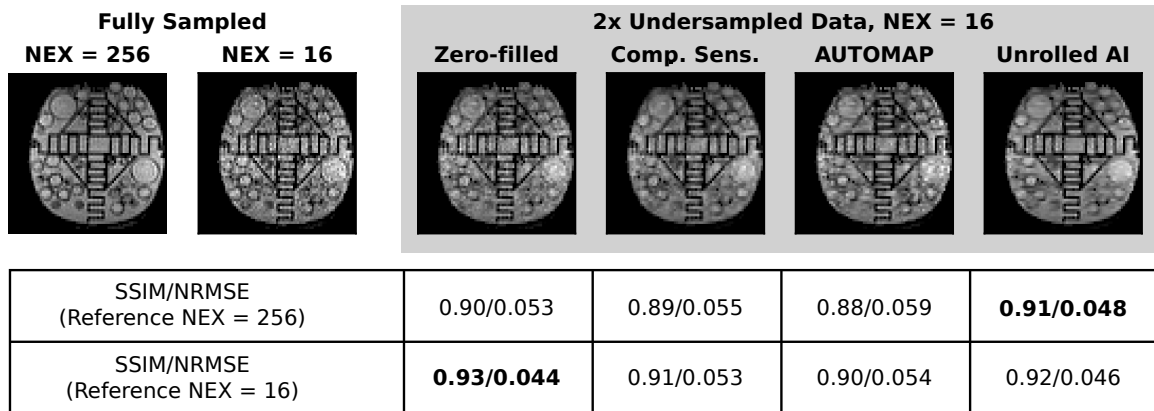


Figure 5: **The hidden noise problem in low-field MRI: computing image-quality metrics (SSIM, NRMSE) using reference images with different levels of noise levels provides highly different results and changes the algorithmic ranking.** The experiment was done using a 6.5 mT scanner and a 3D phantom; a middle slice from the phantom is displayed. Two different reference images were created by acquiring two fully-sampled datasets where the number of excitations (NEX) was 16 and 256. Then, images were reconstructed using the IFFT. Notice that the NEX=16 image contains much more noise than the NEX=256 one. To evaluate the reconstruction methods, the NEX=16 data were retrospectively undersampled with an $R = 2$ Poisson-disc mask and reconstructed with four methods: zero-filled inverse fast Fourier transform (IFFT), Compressed Sensing, AUTOMAP, and the unrolled network. The SSIM and NRMSE metrics were calculated relative to the two fully-sampled reference images, for all the pixels in the 3D volume. The table shows the results for both cases. Notice how the ranking of the ‘best’ result (highlighted in bold) is strongly influenced by the reference image choice.

Comparison for retrospectively undersampled raw data from high- and low-field MRI Scans

Mindful that repurposing publicly available datasets (e.g. fastMRI) for testing AI methods can lead to overly optimistic results (47), we now extend our study to include raw k -space data from 3D human brain scans on 6.5 mT and 3 T MRI scanners. Data from both scanners were acquired with a fully-sampled balanced steady-state free precession (bSSFP) sequence, a popular sequence for low-field acquisitions due to the comparatively high SNR obtained per unit time (60). We emphasize that all data were collected using a single-channel head coil, and the only pre-processing applied before reconstruction was a linear scaling to normalize the k -space magnitude, and, in the 3 T case, cropping k -space to the same matrix size as 6.5 mT data (see Materials and Methods for further details).

The raw k -space data were retrospectively undersampled with Poisson disc masks ($R = 2$), and images were reconstructed using the four methods described above. We observe from the results (Figure 6) that CS, AUTOMAP, and the unrolled AI method reconstruct very similar images for the 3 T data. Those images are free of noise and undersampling artifacts. In contrast, for the 6.5 mT data, the zero-filling, CS, and AUTOMAP methods produce reconstructions with noise and artifacts (see arrows in Figure 6), which indicates that they are not fully robust at low SNR as they are in high-field MRI. The unrolled AI method, on the other hand, provides an artifact-free denoised image with clear edges. In agreement with this visual perception, this method obtains the best NRMSE metric. However, the SSIM metric is the highest for the zero-filled IFFT method, despite the presence of significant noise and aliasing artifacts seen for this method at 6.5 mT. This is likely due to underlying hidden noise in the reference image, as discussed in the previous section. This experiment hence demonstrates the importance of experimentally testing the reconstruction methods, given that artifacts were not present in the fastMRI experiment shown above (Figure 4). Furthermore, it demonstrates the hidden noise problem for raw human-brain MRI data.

Significant differences in image contrast are seen between the bSSFP brain images acquired at 6.5 mT and 3 T (Fig. 6). These contrast differences largely stem from the increase in T_2 relaxation times observed in the ultra-low field regime and the T_2/T_1 -weighting of bSSFP sequences (61). Likely, the reduced performance of the data-driven AUTOMAP reconstruction method has resulted from a shift between training and testing domains, which can be caused by changes in image contrast (62). Model-driven AI methods, such as our unrolled AI approach, are frequently found to be more robust to these domain shifts (63). In Supplementary Figure 3, we also show that the unrolled AI method robustly reconstructs data acquired with gradient echo (GRE) and Magnetization Prepared Rapid Gradient Echo Imaging (MPRAGE) sequences at 3 T; those sequences are pillars of clinical imaging.

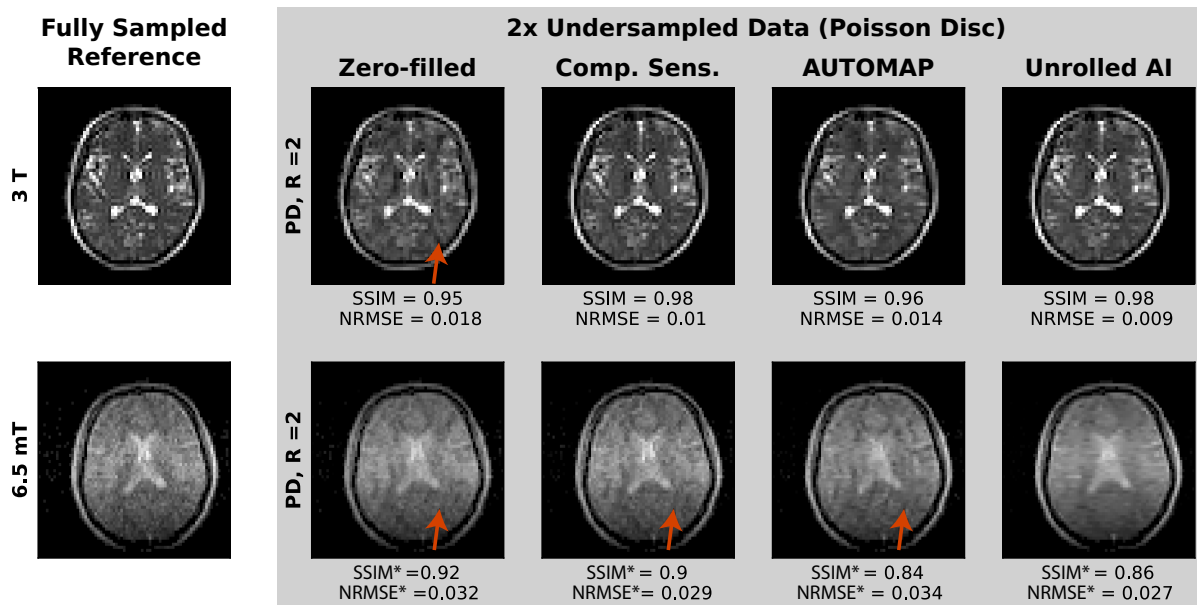


Figure 6: **Experimental comparison of reconstruction methods at high and low magnetic fields.** Fully-sampled, single-channel data from the same healthy subject were acquired at 3 T and 6.5 mT. A Poisson Disc mask ($R = 2$) was retrospectively applied to the k -space data. Compressed sensing (CS), AUTOMAP, and unrolled AI reconstructions were effective at 3 T. In contrast, only the unrolled AI removed undersampling artifacts (red arrows) at 6.5 mT. Normalized root-mean-square error (NRMSE) and Structural similarity (SSIM) values are starred (*) for 6.5 mT images to indicate that the values should be interpreted with caution due to noise present in the fully-sampled reference.

Evaluation for prospectively undersampled ultra-low-field data

Our final experiment demonstrates reconstruction performance for *prospectively undersampled* ultra-low-field data acquired in phantom and in-vivo brain scans using our 6.5 mT MRI scanner. The raw k -space data were acquired with prospectively deployed Poisson disc masks that provided acceleration factors of $R = 2$ and 4. The zero-filled, CS, AUTOMAP, and unrolled AI methods were applied for image reconstruction. For comparison, we also acquired fully-sampled reference data. All scans were acquired independently with $\text{NEX} = 48$, so that the accelerated acquisitions were completed in half or a quarter of the fully-sampled time for $R = 2$ and $R = 4$ masks, respectively.

The results of the phantom scan are shown in Figure 7a. Consistent with the results presented thus far, the unrolled AI method produced the most high-quality images, with sharper edges and less noise than the competing approaches. Specifically, for $R = 4$, the CS and AUTOMAP methods yielded blurry images.

The images reconstructed from prospectively undersampled human brain 6.5 mT data are shown in Figure 7b. Notably, anatomical structures such as the dura and ventricles appear sharpest in the images reconstructed with the unrolled AI network. We visually observe that both AUTOMAP and the unrolled AI methods produced images with less noise compared to the more traditional methods, yet the unrolled AI method did not blur the image to the same extent as AUTOMAP.

It is worth noting that motion artifacts are observed in the fully-sampled reference image, where 44 minutes were required for acquisition. In contrast, motion artifacts are not seen in the reconstructions from accelerated scans, where the acquisitions required ~ 22 minutes for the $2\times$ accelerated scan and ~ 11 minutes for the $4\times$ accelerated one. This indicates improved subject compliance and reduced probability of motion in shorter scans. Therefore, in addition to demonstrating the reconstruction methods for prospectively undersampled data, this experiment also emphasizes the importance of accelerating low-field MRI scans, which currently suffer from excessive scan durations.

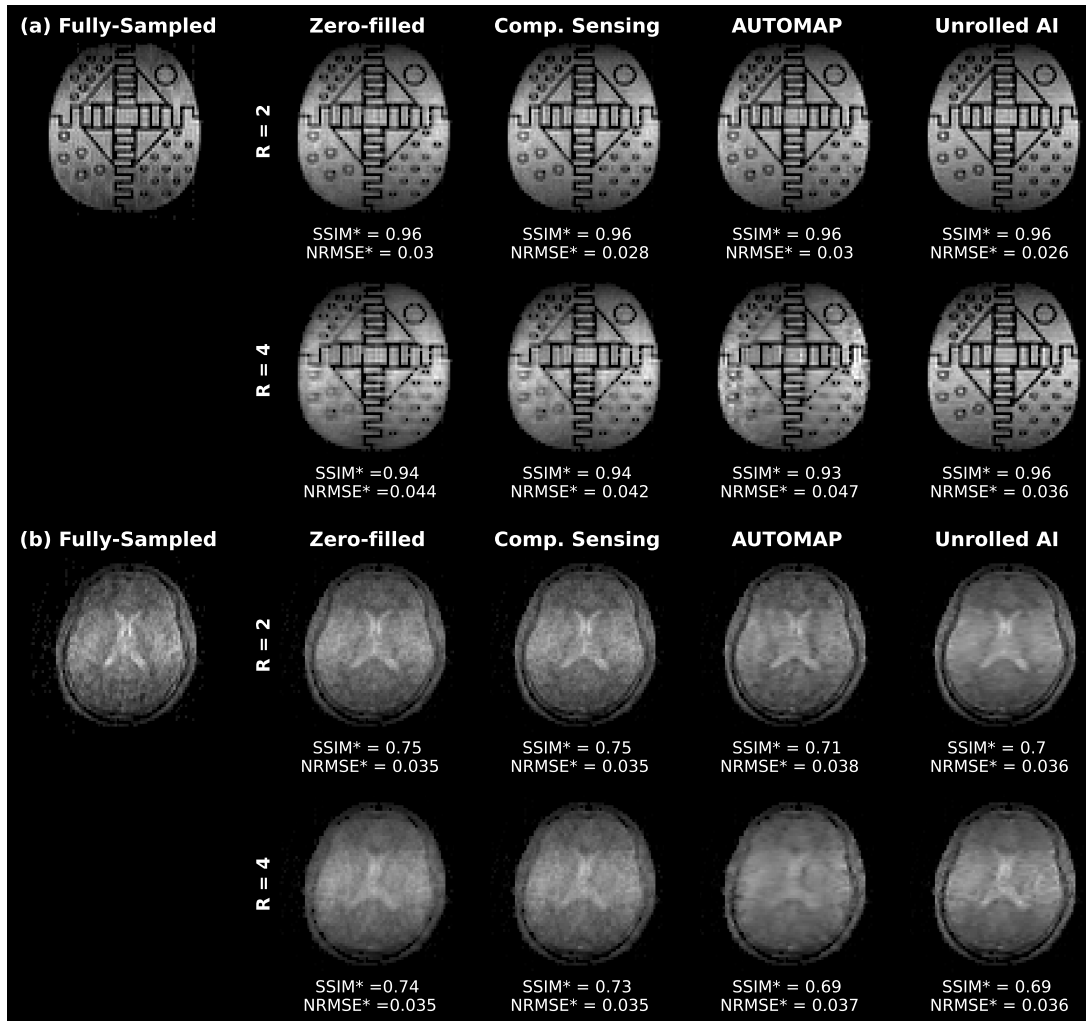


Figure 7: **Reconstruction of prospectively undersampled, raw k -space data acquired with ultra-low-field MRI.** Poisson disc masks with $R = 4$ and $R = 4$ undersampling factors were deployed to a 6.5 mT MRI scanner and used to image a phantom and a human brain, as shown in **a** and **b** respectively. Normalized root-mean-square error (NMRSE) and structural similarity (SSIM) were calculated relative to fully-sampled images that were independently acquired with the same number of excitations (NEX). Phantom scans (NEX=48) took 34 min., 17 min. and 8.5 min for fully-sampled, $R = 2$ and $R = 4$ scans, respectively. Brain scans (NEX=64) took 44 min., 22 min. and 11 min. for fully-sampled, $R = 2$ and $R = 4$ scans, respectively. Image slices from volumes reconstructed with Zero-filled Inverse Fast Fourier Transform, Compressed Sensing, AUTOMAP, and the unrolled AI techniques are shown. Quantitative image quality metrics are starred (*) to indicate that the values should be interpreted with caution due to hidden noise present in the fully-sampled reference. Note that the unrolled AI produces the sharpest results in all cases.

Discussion

Emerging low-field MRI technologies offer considerable potential due to low cost and portability. However, the adoption of low-field MRI is limited by low SNR and long scan duration. While CS and AI reconstruction frameworks can enable substantial scan-time acceleration, as demonstrated by extensive research on high-field MRI (20, 21, 23, 24, 64–66), their application to low-field MRI is in its infancy. Furthermore, given the variability in low-field MRI hardware settings, acquisition protocols, and potential imaging sites (4, 19, 67), a major challenge is that the SNR can fluctuate significantly across scans and locations. Although recent studies analyzed sensitivities of reconstruction methods to data deviations in high field (44–46), their robustness to the SNR changes that characterize low-field MRI has not been explored yet.

To address these key gaps, we conducted a comprehensive evaluation of CS and AI reconstruction frameworks across different datasets, acceleration factors, and a broad range of SNR values, including demonstrations with raw data from high-field (3 T) and ultra-low-field (6.5 mT) scans. We also explored different sampling strategies that better exploit the scan repetition (NEX) dimension for scan acceleration and image quality improvement. Furthermore, in light of recent studies that highlighted critical issues in the evaluation of reconstruction methods due to subtle processes that impact the reference data (44, 47, 51), we conducted the first study demonstrating the ‘hidden noise problem’ in low-field MRI.

Efficient sampling: exploring strategies in the Fourier-NEX domain. Low- and especially ultra-low-field MRI scans commonly involve many repetitions, to improve SNR via k -space data averaging. However, the scan-repetition (NEX) dimension is rarely considered when optimizing k -space sampling patterns, as such repetitions are not common in high-field MRI. Here we explored several approaches for distributing the samples in a domain that consists of k -space and NEX dimensions to optimize the image quality within a fixed scan time ‘budget’. The results indicate that a strategy that combines k -space undersampling, scan repetitions, and CS reconstruction can provide better image quality than a fully-sampled acquisition followed by IFFT reconstruction (Figure 2). Furthermore, we found that using a Poisson Disc undersampling mask provides better results than a Solid Disc mask with equal acceleration. Moreover, our experiments indicate that the combined approach of undersampling, NEX, and CS provides highly robust performance across a wide SNR spectrum. Our findings are in agreement with those of Schoormans et al. (68), who recently explored similar approaches. However, as their work focused on high-field MRI and did not consider stability with respect to SNR changes, our study offers broader insights regarding challenges typical to low-field MRI.

Robustness of reconstruction frameworks for low-field MRI. We conducted a comprehensive evaluation of three well-established reconstruction frameworks—CS, data-driven AI (AUTOMAP), and physics-guided unrolled networks—and analyzed their performance across various settings, including different acceleration factors and a wide range of SNR values. This included retrospective experiments with low-field MRI data synthesized from the fastMRI database (Figures 3 and 4) and experiments with raw MRI data acquired using our high-field (3 T) and ultra-low-field (6.5 mT) MRI systems (Figures 6 and 7).

Our results lead to several key findings. First, we found that physics-guided unrolled neural networks systematically outperform the CS and data-driven AI frameworks for low-field MRI. This is in line with the results of high-field MRI studies, which also identified that unrolling iterative optimization algorithms into a deep network and incorporating data consistency blocks can provide superior performance to purely data-driven approaches (23, 65, 69). However, to the best of our knowledge, this is the first study to conduct this comparison for low-field MRI.

A second key finding of our work is that the unrolled AI method reliably removes undersampling artifacts in low-field imaging and is robust to various data types, acceleration factors, and SNR levels (Figures 2 to 7). Specifically, the results indicate that this framework provides high robustness across the SNR spectrum (Figure 2). Moreover, the unrolled AI not only achieves the best image-quality metrics but is also the only method among those studied here to exhibit a decrease in the metrics' standard deviation with the SNR level (Figure 3), i.e., reconstruction improvement with SNR increase. The CS and AUTOMAP frameworks did not exhibit this behavior; this indicates less stable performance.

Another finding is that CS and AUTOMAP provide relatively similar performance, both quantitatively and visually (Figures 3, 4, 5, and 7), but their relative ranking is inconsistent and depends on both the acceleration factor and SNR level. For example, when testing reconstruction algorithms on $2\times$ undersampled real-world data from 6.5 mT and 3 T MRI scanners, we found that CS outperforms AUTOMAP, but experiments with fastMRI data led to the opposite results.

Relation to previous CS and AI studies. As mentioned above, although CS and AI were largely explored for high-field MRI, their research for low-field imaging remains quite limited. For example, CS has been explored in a few previous studies, e.g. in the context of Overhauser-enhanced MRI (25, 70), but in that application, the SNR is inherently higher by several magnitudes of order compared to standard low-field MRI. Another recent study utilized CS but focused mostly on image distortion correction due to gradient nonlinearity and magnetic field inhomogeneity (27). Furthermore, while these studies are valuable, they did not evaluate CS performance across varying SNR levels, thus our research provides a more comprehensive perspective that can guide future advancements.

Additionally, the development of AI methods for low-field MRI has mostly focused on image-processing tasks, e.g., super-resolution and denoising (33, 35, 37, 42, 71, 72). In contrast, we focused on utilizing AI for image reconstruction from undersampled data. While several recent studies explored this approach (40, 41), the study of Man *et. al* (41) utilized traditional partial-Fourier sampling, which provides only limited acceleration, while that of Zhou *et. al* (40) utilized non-Cartesian spiral acquisition, which is less common in clinical scans. Here we focused on Cartesian acquisitions, which are pillars of clinical MRI. Moreover, we investigated the use of variable-density undersampling schemes (e.g., Poisson Disc sampling), which introduce incoherent artifacts and are hence highly suitable for optimization-based techniques such as CS and AI methods (20, 21, 23, 24, 64).

AUTOMAP (54) has been studied previously for boosting SNR in low-field imaging (42). Although it has demonstrated superior performance to other image reconstructions, our thor-

ough evaluation indicates that its robustness is setting dependent. A possible explanation is that AUTOMAP is a data-driven method, hence it is less robust to domain shifts than competing physics-guided methods (63).

The hidden noise problem in low-field MRI. A recent line of work studied instabilities and sensitivities of CS and AI reconstruction methods to different input-data features (44, 45, 47, 51, 73). Specifically, two studies have raised issues regarding the common use of reference-based image-quality metrics for evaluation of reconstruction algorithms. We have shown that such error metrics could produce biased, overly optimistic results in retrospective sampling experiments where the underlying data are obtained from public databases due to hidden data-preprocessing pipelines that change the data features (47). Additionally, Wang *et. al* (51) have studied parallel (multi-coil) MRI reconstruction and demonstrated that when a root sum-of-squares image is used as a reference, the ‘hidden noise’ in that image can impact the image reconstruction assessment and lead to incorrect algorithmic ranking. Despite the critical implications of these studies, and although low-field MRI is characterized by high levels of noise, to the best of our knowledge such studies have not been undertaken for this domain.

Here, we conducted the first study of the ‘hidden noise’ problem in low-field MRI. Specifically, we acquired data using a 6.5 mT scanner and computed two reference images, corresponding to averages of NEX=16 and NEX=256 datasets. Naturally, the latter contained less noise due to the higher number of acquisitions. We then computed reconstructions for $2\times$ undersampled data using the reconstruction methods studied here (zero-filling, CS, AUTOMAP, and unrolled AI) and quantified their performance using each reference image separately. The results (see table in Figure 5) indicated that using a reference image with a high level of noise can produce a misleading algorithmic ranking. Therefore, in agreement with (47, 51), our study demonstrates that a careless choice of reference data can lead to unreliable algorithmic ranking. If algorithms are chosen based on such ranking, this can later lead to sub-optimal performance in clinical settings. Therefore, we believe it is important to raise awareness of this problem. Strategies for mitigating this issue can include, for example, the use of noise augmentation during the AI training process (73), the use of noise-aware image quality metrics such as noncentral chi error metric proposed in Ref. 51, and SNR-aware hardware engineering (67).

Methods evaluation on real-world prospectively acquired low-field MRI data. The first part of our work (Figures 2 to 3) was performed using low-field data synthesized from the high-field fastMRI database (52). To validate that our results are not specific to this ‘fastMRI domain’, we deployed our models on raw experimental data acquired in low- and high-field scans (Figures 4 to 7). Experiments were done using retrospective undersampling and with data acquired with prospective undersampling. The results confirmed our previous findings: the unrolled AI method provided the most high-quality results, for all the examined field strengths, data types, and acceleration factors. Notably, for some of the 6.5 mT brain MRI data (Figure 6), *only* the unrolled AI method was able to remove undersampling artifacts while also maintaining image sharpness; this indicates the powerful capabilities of this approach.

Limitations and future work. In this study, we have analyzed only single-coil acquisitions, as those characterize many low-field MRI systems (2, 19), including our 6.5 mT system (1). As

single-coil acquisitions enable only moderate acceleration factors, we focused on the regime of $2\times$ to $4\times$ acceleration. Although a study demonstrating multi-coil low-field MRI was recently published (40), such datasets are not available online, hence the extension of the current research to multi-coil settings is beyond the scope of this work. Furthermore, there is a notable scarcity of public datasets offering low-field MRI data (74), with M4Raw (75) currently being the only database in this regime. Therefore, future development of multi-coil low-field MRI systems and the creation of further databases can enable extending our work to other settings.

In summary, this study aims to provide novel insights regarding advanced image reconstruction frameworks for low-field MRI. Our work focused on analyzing the robustness of CS and AI frameworks to various acceleration factors and SNR fluctuations. Furthermore, we demonstrated the ‘hidden noise’ problem in low-field MRI and highlighted critical issues underlying reliable algorithmic evaluation in high-noise settings. Our findings and insights can inform the development of future acquisition-reconstruction strategies for faster, high-quality imaging methods and optimized workflows, which are highly needed for clinical low-field MRI (66). Moreover, potential future studies can expand the scope from diagnostic portable MRI systems to real-time therapy guidance. There is increasing demand for accelerated imaging on low-field MRI systems used for therapy guidance, especially within interventional radiology (76) and MRI-guided radiotherapy domains (77, 78).

Materials and Methods

Data Acquisition

Data preprocessing for *in silico* experiments

To generate large training, validation, and testing datasets of high-SNR images, data from fastMRI were preprocessed to resemble single-channel k -space data acquired on our 6.5 mT MRI scanner (52). Specifically, multi-channel, fully-sampled raw k -space data were sourced from the FastMRI brain training and validation datasets, yielding thousands of 1.5 T / 3 T scans. Coil sensitivity maps were calculated using the ESPIRiT algorithm and SigPy (79, 80) and used for combining the multi-channel IFFT-reconstructed images into complex-valued, single-channel images. Reconstructed brain volumes were converted to 3D k -space via FFT and downsampled to the ultra-low field resolution of $64 \times 75 \times 25$ via k -space cropping. Ground-truth reference images were obtained via IFFT reconstruction of those downsampled k -space data. Finally, the brain volumes were split into training, validation and test datasets containing 3300, 1100 and 100 volumes respectively.

The training data were further supplemented by 50,000 brain image slices sourced from the Human Connectome Project (HCP) (81). These brain images were derived from DICOM magnitude images and had synthetic phase maps applied to synthesize complex data acquisition. Individual image slices were downsampled to 75×25 via k -space cropping to match the resolution of ultra-low field acquisitions. The synthesis of this HCP dataset is fully described

in Reference 42. We emphasize that this dataset was used only for training, i.e. it served as an augmentation method, and not for testing the algorithms.

To analyse the impact of SNR on image-reconstruction performance, for all datasets the downsampled k -space data were degraded through the addition of complex-valued additive white Gaussian noise at varying noise power. SNR scales approximately as $B_0^{\frac{3}{2}}$ (18). We tested a wide range of SNR values (40 dB range shown in Fig. 2 and Fig. 3) as the variation in SNR expected between clinical and low-field MRI scanners can be very large. Additionally, all images and k -space data were linearly scaled such that the 95th percentile of pixel intensity in IFFT reconstructed images was set to 1. This intensity scaling is a standard approach in AI methods for MRI reconstruction.

Ultra-low Field MRI Experiments

Imaging experiments were performed on a 6.5 mT MRI scanner that consists of a biplanar electromagnet-based scanner with a peak gradient strength of 1 mT/m (I). Image data were acquired in compliance with Institutional Review Board (IRB) approvals with a custom quadrature head coil that has been described previously (82). Data from this quadrature coil were digitized as two-channel data and then linearly summed after applying a $\pi/2$ phase shift to k -space data from the second channel.

A 3D Cartesian balanced-steady state free precession (bSSFP) sequence with TR/TE = 22/11 ms and matrix size $64 \times 75 \times 25$ (Readout \times Phase Encode 1 \times Phase Encode 2) was programmed with a Tecmag Restone spectrometer and used for data acquisition. These parameters gave a voxel size on the 6.5 mT scanner of $2.5 \text{ mm} \times 3.5 \text{ mm} \times 8 \text{ mm}$ (RO \times PE1 \times PE2). The number of excitations (NEX) was varied as described in the Results section.

For prospectively undersampled acquisitions, Poisson disc masks with acceleration factors of $R = 2$ and $R = 4$ were exported from SigPy and used to populate the phase encoding tables on the spectrometer prior to acquisition. Fully-sampled acquisitions were captured in the same imaging session for comparison of reconstruction methods.

MRI at 3T

High-field imaging data were collected in compliance with IRB approvals from a healthy volunteer on a 3 T Siemens Skyra scanner. A single-channel head coil and a 3D bSSFP sequence (known as True Fast Imaging with Steady-State Free Precession or TRUFI on Siemens scanners) were used for data acquisition. The 3 T bSSFP data shown in Figure 6 were acquired with TR/TE = 4.8 ms/2.4 ms and a matrix size of $256 \times 256 \times 128$ (Readout \times Phase Encode 1 \times Phase Encode 2) in the anterior-posterior, left-right and superior-inferior directions, respectively. Fully-sampled data were retrospectively downsampled via k -space cropping to the same resolution used at ultra-low field ($64 \times 75 \times 25$).

Fully-sampled data were additionally acquired with gradient-recalled echo (GRE) and Magnetization Prepared Rapid Gradient Echo (MPRAGE) sequences using TR/TE values of 8 ms/2.3 ms

and 2300 ms/4.4 ms, respectively. Downsampling was performed using the same k -space cropping methodology and the results of reconstruction tests performed using these data are shown in Supplementary Figure 3.

Image Reconstruction

Retrospective undersampling

For retrospective undersampling experiments, 2D masks were created in Python using Sigpy (80) and then applied to fully-sampled data in both phase encode directions. Poisson-disc masks were created using the corresponding tool in Sigpy, with a 10×10 fully-sampled region added to the centre. Undersampling factors were increased to ensure the reported acceleration factors (2 or 4) were accurate after addition of this fully-sampled region.

IFFT and CS reconstructions

Fully-sampled data were reconstructed using a conventional IFFT operation. For undersampled data, missing k -space data entries were first zero-filled, and images were then reconstructed via IFFT. The zero-filled data were also used as a starting point for $l1$ -wavelet CS reconstruction, using the Sigpy package (80). The CS regularization parameter (λ) was optimized for each dataset and acceleration factor separately by performing a grid search over the range of $[10^{-6}$ - $10^{-1}]$. The iteration number used for the reconstructions was then optimized over the range $[1$ - $200]$.

For experiments using the fastMRI dataset, the optimal λ and iteration numbers for CS reconstruction were calculated as the values that minimized the mean NRMSE across 20 brain volumes drawn from the validation set as compared to the ground truth image. Values were reoptimized for each variation in input SNR. For retrospective and prospective experiments on our MRI scanners, the λ and iteration values were chosen to minimize NRMSE relative to the fully-sampled image. This parameter re-optimization means that the CS algorithm is being evaluated in terms of its ‘best possible performance’ in each experiment.

AI methods implementation

AUTOMAP: The AUTOMAP reconstruction framework was implemented using supervised learning in Keras and TensorFlow (42, 62). The AUTOMAP network architecture comprises six trainable layers. The first two layers are fully-connected (dense) layers with hyperbolic tangent activations, which process the flattened input data through hidden layers. The data are then reshaped into a matrix format before passing through three convolutional layers. The first convolutional layer has 128 filters with a 5×5 kernel and uses a hyperbolic tangent activation function. The second and third convolutional layers each have 128 filters with 5×5 kernels and utilize rectified linear unit (ReLU) activation functions. Finally, a transposed convolutional layer with a single filter and a 5×5 kernel generates the final image. This architecture enables

the network to learn the spatial decoding process between k -space and image space without any prior knowledge. The AUTOMAP network contains 21,925,360 trainable parameters for the 75×25 input size. Visual descriptions of the AUTOMAP architecture were provided in References 42, 54, 62.

Unrolled AI: Our unrolled AI approach to image reconstruction was implemented in PyTorch. The Unrolled architecture consists of 10 iterative soft shrinkage-thresholding blocks. Each block begins with a data fidelity calculation, followed by nonlinear transforms and a soft thresholding operation. The nonlinear transforms include forward and backward operations, each designed as a combination of two convolutional layers split by a rectified linear unit (ReLU). A skip connection is incorporated to form a residual block, aiding in network training. A data consistency operation is included at the end of each block (except for the final block) to ensure k -space consistency with the measured k -space samples. This data consistency layer replaces AI-generated k -space data with the original data at sampled points. In the last iteration, the data consistency block is omitted to allow the convolutional layers to denoise the original low SNR k -space data that was reinjected in previous iterations. As implemented, the Unrolled network has 98,760 parameters, a value that is not dependent on the input size. The full Unrolled network architecture is detailed in Reference 63.

Training: Both image reconstruction networks were trained using the same training corpus of fastMRI and HCP data described above. To minimize graphical processing unit (GPU) memory requirements, networks were trained to reconstruct 2D, rather than 3D, data (83). Hence, the training corpus was utilized as a stack of independent 2D 75×25 brain image/masked k -space pairs. Data were further augmented by adding random amounts of synthetic Gaussian noise to the input during training, with a variable magnitude range that mimicked the SNR expected during implementation. Individual networks were trained for each undersampling mask.

A custom loss function was defined to calculate the mean square error (MSE) with the background region outside the brain/head masked. This masking encourages the neural networks to focus on improving image structure within the brain rather than denoising the background (84). Masking was performed in regions where the normalized reference images had a signal magnitude less than 0.005.

Each network was trained for up to 100 epochs. AUTOMAP training utilized a learning rate of 0.0001 and the RMSprop optimizer. Unrolled AI networks were trained with a learning rate of 0.001 and the Adam optimizer.

Two separate AUTOMAP networks were trained for each reconstruction task, one to reconstruct real image data and one to reconstruct imaginary image data. AUTOMAP networks received the same complex k -space input data but were shown different (real or imaginary) reference images.

Loss functions. Additional experiments were performed to test the effects of perceptual loss functions during training (59). Results from these experiments are reported in Supplementary Figure 2. To train the unrolled network, we utilized the Learned Perceptual Image Patch Similarity (LPIPS) loss available for PyTorch at <https://github.com/richzhang/PerceptualSimilarity>. To train AUTOMAP, we ported this LPIPS loss to TensorFlow.

Our implementation is available at:

https://github.com/Image-X-Institute/lpips_torch2tf (85).

Inference. All reconstructions presented in the Results section were performed on 3D k -space data. To address GPU memory limitations, a 1D FFT was first applied along the fully-sampled readout dimension of k -space to yield a stack of hybrid k -space data. The trained networks were then applied to the hybrid k -space data to perform reconstruction in undersampled phase encode directions via inference. In the case of AUTOMAP, inference was performed separately with real and imaginary networks before outputs were combined into a complex image.

Metric Calculations

Maximum-minimum normalized root-mean-square error (NRMSE), and structural similarity index (SSIM) metrics were calculated relative to a fully-sampled reference image (86). Regions outside the brain/phantom that should not contain any MRI signal were excluded from metric calculations by calculating a binary mask on the fully-sampled reference image. By excluding the background from metric calculations, algorithms that better recover structures within the region of interest are ranked more highly.

References and Notes

1. M. Sarracanie, C. D. Lapierre, N. Salameh, D. E. J. Waddington, T. Witzel, M. S. Rosen, Low-Cost High-Performance MRI. *Sci. Rep.* **5**, 15177-15177 (2015).
2. J. P. Marques, F. F. J. Simonis, A. G. Webb, Low-field MRI: An MR physics perspective. *Journal of Magnetic Resonance Imaging* **49**, 1528-1542 (2019).
3. L. L. Wald, P. C. McDaniel, T. Witzel, J. P. Stockmann, C. Z. Cooley, Low-cost and portable MRI. *J Magn Reson Imaging* **52**, 686-696 (2020).
4. W. T. Kimberly, A. J. Sorby-Adams, A. G. Webb, E. X. Wu, R. Beekman, R. Bowry, S. J. Schiff, A. de Havenon, F. X. Shen, G. Sze, P. Schaefer, J. E. Iglesias, M. S. Rosen, K. N. Sheth, Brain imaging with portable low-field MRI. *Nat Rev Bioeng* **1**, 617-630 (2023).
5. Y. Liu, A. T. L. Leong, Y. Zhao, L. Xiao, H. K. F. Mak, A. C. O. Tsang, G. K. K. Lau, G. K. K. Leung, E. X. Wu, A low-cost and shielding-free ultra-low-field brain MRI scanner. *Nature Communications* **12** (2021).
6. Y. Zhao, Y. Ding, V. Lau, C. Man, S. Su, L. Xiao, A. T. L. Leong, E. X. Wu, Whole-body magnetic resonance imaging at 0.05 Tesla. *Science* **384** (2024).

7. A. S. Shetty, D. R. Ludwig, J. E. Ippolito, T. J. Andrews, V. R. Narra, T. J. Fraum, Low-Field-Strength Body MRI: Challenges and Opportunities at 0.55 T. *RadioGraphics* **43** (2023).
8. N. Salameh, D. J. Lurie, O. Ipek, C. Z. Cooley, A. E. Campbell-Washburn, Exploring the foothills: benefits below 1 Tesla? *Magnetic Resonance Materials in Physics, Biology and Medicine* **36**, 329-333 (2023).
9. S. S. Bhat, T. T. Fernandes, P. Poojar, M. da Silva Ferreira, P. C. Rao, M. C. Hanumantharaju, G. Ogbole, R. G. Nunes, S. Geethanath, Low-Field MRI of Stroke: Challenges and Opportunities. *Journal of Magnetic Resonance Imaging* **54**, 372-390 (2020).
10. M. H. Mazurek, B. A. Cahn, M. M. Yuen, A. M. Prabhat, I. R. Chavva, J. T. Shah, A. L. Crawford, E. B. Welch, J. Rothberg, L. Sacolick, M. Poole, C. Wira, C. C. Matouk, A. Ward, N. Timario, A. Leasure, R. Beekman, T. J. Peng, J. Witsch, J. P. Antonios, G. J. Falcone, K. T. Gobeske, N. Petersen, J. Schindler, L. Sansing, E. J. Gilmore, D. Y. Hwang, J. A. Kim, A. Malhotra, G. Sze, M. S. Rosen, W. T. Kimberly, K. N. Sheth, Portable, bedside, low-field magnetic resonance imaging for evaluation of intracerebral hemorrhage. *Nature Communications* **12**, 5119-5119 (2021).
11. J. Obungoloch, J. R. Harper, S. Consevage, I. M. Savukov, T. Neuberger, S. Tadigadapa, S. J. Schiff, Design of a sustainable prepolarizing magnetic resonance imaging system for infant hydrocephalus. *MAGMA* **31**, 665-676 (2018).
12. M. M. Yuen, A. M. Prabhat, M. H. Mazurek, I. R. Chavva, A. Crawford, B. A. Cahn, R. Beekman, J. A. Kim, K. T. Gobeske, N. H. Petersen, G. J. Falcone, E. J. Gilmore, D. Y. Hwang, A. S. Jasne, H. Amin, R. Sharma, C. Matouk, A. Ward, J. Schindler, L. Sansing, A. de Havenon, A. Aydin, C. Wira, G. Sze, M. S. Rosen, W. T. Kimberly, K. N. Sheth, Portable, low-field magnetic resonance imaging enables highly accessible and dynamic bedside evaluation of ischemic stroke. *Science Advances* **8** (2022).
13. P. Laso, S. Cerri, A. Sorby-Adams, J. Guo, F. Mateen, P. Goebel, J. Wu, P. Liu, H. B. Li, S. Young, Quantifying white matter hyperintensity and brain volumes in heterogeneous clinical and low-field portable MRI. *2024 IEEE International Symposium on Biomedical Imaging (ISBI)* (2024), pp. 1–5.
14. A. de Havenon, N. R. Parasuram, A. L. Crawford, M. H. Mazurek, I. R. Chavva, V. Yadlapalli, J. E. Iglesias, M. S. Rosen, G. J. Falcone, S. Payabvash, G. Sze, R. Sharma, S. J. Schiff, B. Safdar, C. Wira, W. T. Kimberly, K. N. Sheth, Identification of White Matter Hyperintensities in Routine Emergency Department Visits Using Portable Bedside Magnetic Resonance Imaging. *Journal of the American Heart Association* **12** (2023).

15. S. Sheng, N. Koonjoo, F. K. Longarino, L. R. Lamb, J. C. Villa Camacho, T. P. Hornung, S. E. Ogier, S. Yan, T. R. Bortfeld, M. A. Saksena, *et al.*, Breast imaging with an ultra-low field MRI scanner: a pilot study. *medRxiv* pp. 2024–04 (2024).
16. L. Broche, V. Mallikourti, P. Ross, K. Hanna, G. Davies, D. Lurie, O. Maier, E. Hussein, G. Lip, H. Lahrech, *et al.*, Field Cycling Imaging: a novel modality to characterise breast cancer at low and ultra-low magnetic fields below 0.2 T. *Research Square (Preprint Server)* pp. doi.org/10.21203/rs.3.rs-3759270/v1 (2024).
17. A. Webb, J. Obungoloch, Five steps to make MRI scanners more affordable to the world. *Nature* **615**, 391–393 (2023).
18. D. I. Hoult, R. E. Richards, The Signal-to-Noise Ratio of the Nuclear Magnetic Resonance Experiment. *J. Magn. Reson.* **24**, 71-85 (1976).
19. T. C. Arnold, C. W. Freeman, B. Litt, J. M. Stein, Low-field MRI: Clinical promise and challenges. *Journal of Magnetic Resonance Imaging* **57**, 25-44 (2022).
20. M. Lustig, D. Donoho, J. M. Pauly, Sparse MRI: The application of compressed sensing for rapid MR imaging. *Magnetic Resonance in Medicine* **58**, 1182-95 (2007).
21. L. Feng, T. Benkert, K. T. Block, D. K. Sodickson, R. Otazo, H. Chandarana, Compressed sensing for body MRI. *Journal of Magnetic Resonance Imaging* **45**, 966–987 (2017).
22. S. Wang, T. Xiao, Q. Liu, H. Zheng, Deep learning for fast MR imaging: A review for learning reconstruction from incomplete k-space data. *Biomedical Signal Processing and Control* **68**, 102579 (2021).
23. K. Hammernik, T. Küstner, B. Yaman, Z. Huang, D. Rueckert, F. Knoll, M. Akçakaya, Physics-Driven Deep Learning for Computational Magnetic Resonance Imaging: Combining physics and machine learning for improved medical imaging. *IEEE signal processing magazine* **40**, 98–114 (2023).
24. R. Heckel, M. Jacob, A. Chaudhari, O. Perlman, E. Shimron, Deep learning for accelerated and robust MRI reconstruction. *Magnetic Resonance Materials in Physics, Biology and Medicine* **37**, 335-368 (2024).
25. M. Sarracanie, B. D. Armstrong, J. Stockmann, M. S. Rosen, High speed 3D overhauser-enhanced MRI using combined b-SSFP and compressed sensing. *Magn. Reson. Med.* **71**, 735-745 (2013).
26. D. Tamada, K. Kose, Two-dimensional compressed sensing using the cross-sampling approach for low-field MRI systems. *IEEE Transactions on Medical Imaging* **33**, 1905-1912 (2014).

27. K. Koolstra, T. O'Reilly, P. Börnert, A. Webb, Image distortion correction for MRI in low field permanent magnet systems with strong B0 inhomogeneity and gradient field nonlinearities. *Magnetic Resonance Materials in Physics, Biology and Medicine* **34**, 631-642 (2021).
28. N. F. Ishak, M. J. Gangeh, R. Logeswaran, Comparison of Denoising Techniques Applied on Low-Field MR Brain Images. *2008 Fifth International Conference on Computer Graphics, Imaging and Visualisation* (2008), pp. 345–349.
29. A. G. Hernandez, P. Fau, S. Rapacchi, J. Wojak, H. Mailleux, M. Benkreira, M. Adel, Improving image quality in low-field MRI with deep learning. *2021 IEEE International Conference on Image Processing (ICIP)* (2021), pp. 260–263.
30. D. B. T. Le, M. Sadinski, A. Nacev, R. Narayanan, D. Kumar, Deep Learning-based Method for Denoising and Image Enhancement in Low-Field MRI. *2021 IEEE International Conference on Imaging Systems and Techniques (IST)* (2021), pp. 1–6.
31. X. Lin, C. Du, Q. Wu, X. Tian, J. Yu, Y. Zhang, H. Wei, Zero-Shot Low-Field MRI Enhancement via Denoising Diffusion Driven Neural Representation. *International Conference on Medical Image Computing and Computer-Assisted Intervention* (Springer, 2024), pp. 775–785.
32. V. Lau, L. Xiao, Y. Zhao, S. Su, Y. Ding, C. Man, X. Wang, A. Tsang, P. Cao, G. K. K. Lau, G. K. K. Leung, A. T. L. Leong, E. X. Wu, Pushing the limits of low-cost ultra-low-field MRI by dual-acquisition deep learning 3D superresolution. *Magnetic Resonance in Medicine* **90**, 400-416 (2023).
33. M. L. de Leeuw den Bouter, G. Ippolito, T. P. A. O'Reilly, R. F. Remis, M. B. van Gijzen, A. G. Webb, Deep learning-based single image super-resolution for low-field MR brain images. *Scientific Reports* **12** (2022).
34. S. Kim, H. F. J. Tregidgo, A. K. Eldaly, M. Figini, D. C. Alexander, A 3D Conditional Diffusion Model for Image Quality Transfer – An Application to Low-Field MRI (2023).
35. K. T. Islam, S. Zhong, P. Zakavi, Z. Chen, H. Kavnoudias, S. Farquharson, G. Durbridge, M. Barth, K. L. McMahan, P. M. Parizel, A. Dwyer, G. F. Egan, M. Law, Z. Chen, Improving portable low-field MRI image quality through image-to-image translation using paired low- and high-field images. *Scientific Reports* **13**, 21183 (2023).
36. A. Lucas, T. C. Arnold, S. V. Okar, C. Vadali, K. D. Kawatra, Z. Ren, Q. Cao, R. T. Shinohara, M. K. Schindler, K. A. Davis, B. Litt, D. S. Reich, J. M. Stein, Multi-contrast high-field quality image synthesis for portable low-field MRI using generative adversarial networks and paired data. *medRxiv* p. 2023.12.28.23300409 (2023).

37. R. Ayde, T. Senft, N. Salameh, M. Sarracanie, Deep learning for fast low-field MRI acquisitions. *Scientific Reports* **12**, 1-13 (2022).
38. M. M. Jimeno, K. S. Ravi, Z. Jin, D. Oyekunle, G. Ogbole, S. Geethanath, ArtifactID: Identifying artifacts in low-field MRI of the brain using deep learning. *Magnetic resonance imaging* **89**, 42–48 (2022).
39. Y. Zhao, L. Xiao, Y. Liu, A. T. Leong, E. X. Wu, Electromagnetic interference elimination via active sensing and deep learning prediction for radiofrequency shielding-free MRI. *NMR in Biomedicine* **37**, e4956 (2024).
40. B. Zhou, J. Schlemper, N. Dey, S. S. M. Salehi, K. Sheth, C. Liu, J. S. Duncan, M. Sofka, Dual-domain self-supervised learning for accelerated non-Cartesian MRI reconstruction. *Medical Image Analysis* **81**, 102538 (2022).
41. C. Man, V. Lau, S. Su, Y. Zhao, L. Xiao, Y. Ding, G. K. Leung, A. T. Leong, E. X. Wu, Deep learning enabled fast 3D brain MRI at 0.055 tesla. *Science Advances* **9**, eadi9327 (2023).
42. N. Koonjoo, B. Zhu, G. C. Bagnall, D. Bhutto, M. S. Rosen, Boosting the signal-to-noise of low-field MRI with deep learning image reconstruction. *Scientific Reports* **11**, 8248-8248 (2021).
43. S. C. L. Deoni, P. Medeiros, A. T. Deoni, P. Burton, J. Beauchemin, V. D'Sa, E. Boskamp, S. By, C. McNulty, W. Mileski, B. E. Welch, M. Huentelman, Development of a mobile low-field MRI scanner. *Scientific Reports* **12**, 5690 (2022).
44. V. Antun, F. Renna, C. Poon, B. Adcock, A. C. Hansen, On instabilities of deep learning in image reconstruction and the potential costs of AI. *Proceedings of the National Academy of Sciences* **117**, 30088–30095 (2020).
45. M. Z. Darestani, A. S. Chaudhari, R. Heckel, Measuring robustness in deep learning based compressive sensing. *International Conference on Machine Learning* (PMLR, 2021), pp. 2433–2444.
46. F. Knoll, K. Hammernik, E. Kobler, T. Pock, M. P. Recht, D. K. Sodickson, Assessment of the generalization of learned image reconstruction and the potential for transfer learning. *Magnetic resonance in medicine* **81**, 116–128 (2019).
47. E. Shimron, J. I. Tamir, K. Wang, M. Lustig, Implicit data crimes: Machine learning bias arising from misuse of public data. *Proceedings of the National Academy of Sciences of the United States of America* **119**, e2117203119 (2022).
48. P. Virtue, M. Lustig, The empirical effect of gaussian noise in undersampled mri reconstruction. *Tomography* **3**, 211–221 (2017).

49. P. Poojar, I. E. Oiyee, K. Aggarwal, M. M. Jimeno, J. T. Vaughan, S. Geethanath, Repeatability of image quality in very low-field MRI. *NMR in Biomedicine* **37**, e5198 (2024).
50. Z. Wang, A. C. Bovik, H. R. Sheikh, E. P. Simoncelli, Image quality assessment: from error visibility to structural similarity. *IEEE transactions on image processing* **13**, 600–612 (2004).
51. J. Wang, D. An, J. P. Haldar, The “hidden noise” problem in MR image reconstruction. *Magnetic Resonance in Medicine* (2024).
52. F. Knoll, J. Zbontar, A. Sriram, M. J. Muckley, M. Bruno, A. Defazio, M. Parente, K. J. Geras, J. Katsnelson, H. Chandarana, Z. Zhang, M. Drozdal, A. Romero, M. Rabbat, P. Vincent, J. Pinkerton, D. Wang, N. Yakubova, E. Owens, C. L. Zitnick, M. P. Recht, D. K. Sodickson, Y. W. Lui, fastMRI: A Publicly Available Raw k-Space and DICOM Dataset of Knee Images for Accelerated MR Image Reconstruction Using Machine Learning. *Radiology: Artificial Intelligence* **2**, e190007-e190007 (2020).
53. D. E. J. Waddington, E. Shimron, N. Hindley, N. Koonjoo, M. S. Rosen, Accelerating Ultra-Low Field MRI with Compressed Sensing. *31st Meeting of the International Society of Magnetic Resonance in Medicine* (2022), p. 1818.
54. B. Zhu, J. Z. Liu, B. R. Rosen, M. S. Rosen, Image reconstruction by domain transform manifold learning. *Nature* **555**, 487-492 (2018).
55. J. Zhang, B. Ghanem, ISTA-Net: Interpretable Optimization-Inspired Deep Network for Image Compressive Sensing. *Proceedings of the IEEE Computer Society Conference on Computer Vision and Pattern Recognition* pp. 1828–1837 (2018).
56. Q. Fan, T. Witzel, A. Nummenmaa, K. R. A. Van Dijk, J. D. Van Horn, M. K. Drews, L. H. Somerville, M. A. Sheridan, R. M. Santillana, J. Snyder, T. Hedden, E. E. Shaw, M. O. Hollinshead, V. Renvall, R. Zanzonico, B. Keil, S. Cauley, J. R. Polimeni, D. Tisdall, R. L. Buckner, V. J. Wedeen, L. L. Wald, A. W. Toga, B. R. Rosen, MGH–USC Human Connectome Project datasets with ultra-high b-value diffusion MRI. *NeuroImage* **124**, 1108-1114 (2016).
57. F. Knoll, K. Hammernik, C. Zhang, S. Moeller, T. Pock, D. K. Sodickson, M. Akcakaya, Deep-Learning Methods for Parallel Magnetic Resonance Imaging Reconstruction: A Survey of the Current Approaches, Trends, and Issues. *IEEE Signal Processing Magazine* **37**, 128-140 (2020).
58. A. Reinke, *et al.*, Understanding metric-related pitfalls in image analysis validation. *Nature Methods* **21**, 182-194 (2024).

59. R. Zhang, P. Isola, A. A. Efros, E. Shechtman, O. Wang, The Unreasonable Effectiveness of Deep Features as a Perceptual Metric (2018). Accepted to CVPR 2018; Code and data available at <https://www.github.com/richzhang/PerceptualSimilarity>.
60. Y. Tian, K. S. Nayak, New clinical opportunities of low-field MRI: heart, lung, body, and musculoskeletal. *Magnetic Resonance Materials in Physics, Biology and Medicine* **37**, 1-14 (2024).
61. D. E. J. Waddington, T. Boele, R. Maschmeyer, Z. Kuncic, M. S. Rosen, High-sensitivity in vivo contrast for ultra-low field magnetic resonance imaging using superparamagnetic iron oxide nanoparticles. *Science Advances* **6**, eabb0998-eabb0998 (2020).
62. D. E. J. Waddington, N. Hindley, N. Koonjoo, C. Chiu, T. Reynolds, P. Z. Y. Liu, B. Zhu, D. Bhutto, C. Paganelli, P. J. Keall, M. S. Rosen, Real-time radial reconstruction with domain transform manifold learning for MRI-guided radiotherapy. *Medical Physics* **50**, 1962-1974 (2023).
63. S. Shan, Y. Gao, P. Z. Y. Liu, B. Whelan, H. Sun, B. Dong, F. Liu, D. E. J. Waddington, Distortion-Corrected Image Reconstruction with Deep Learning on an MRI-Linac. *Magnetic Resonance in Medicine* **90**, 963-977 (2023).
64. J. Fessler, Model-Based Image Reconstruction for MRI. *IEEE Signal Processing Magazine* **27**, 81-89 (2010).
65. K. Hammernik, T. Klatzer, E. Kobler, M. P. Recht, D. K. Sodickson, T. Pock, F. Knoll, Learning a variational network for reconstruction of accelerated MRI data. *Magnetic resonance in medicine* **79**, 3055–3071 (2018).
66. E. Shimron, O. Perlman, AI in MRI: Computational frameworks for a faster, optimized, and automated imaging workflow (2023).
67. A. Webb, T. O'Reilly, Tackling SNR at low-field: a review of hardware approaches for point-of-care systems. *Magnetic Resonance Materials in Physics, Biology and Medicine* **36**, 375–393 (2023).
68. J. Schoormans, G. J. Strijkers, A. C. Hansen, A. J. Nederveen, B. F. Coolen, Compressed sensing MRI with variable density averaging (CS-VDA) outperforms full sampling at low SNR. *Physics in Medicine and Biology* **65**, 045004 (2020).
69. H. K. Aggarwal, M. P. Mani, M. Jacob, MoDL: Model Based Deep Learning Architecture for Inverse Problems. *IEEE Transactions on Medical Imaging* **38**, 394-405 (2019).
70. D. E. J. Waddington, M. Sarracanie, N. Salameh, F. Herisson, C. Ayata, M. S. Rosen, An Overhauser-enhanced-MRI platform for dynamic free radical imaging in vivo. *NMR in Biomedicine* **31**, e3896-e3896 (2018).

71. J. E. Iglesias, R. Schleicher, S. Laguna, B. Billot, P. Schaefer, B. McKaig, J. N. Goldstein, K. N. Sheth, M. S. Rosen, W. T. Kimberly, Quantitative Brain Morphometry of Portable Low-Field-Strength MRI Using Super-Resolution Machine Learning. *Radiology* **306**, e220522 (2023).
72. R. Ayde, M. Vornehm, Y. Zhao, F. Knoll, E. X. Wu, M. Sarracanie, MRI at low field: A review of software solutions for improving SNR. *NMR in Biomedicine* (2024).
73. A. D. Desai, B. M. Ozturkler, C. M. Sandino, R. Boutin, M. Willis, S. Vasanaawala, B. A. Hargreaves, C. Ré, J. M. Pauly, A. S. Chaudhari, Noise2Recon: Enabling SNR-robust MRI reconstruction with semi-supervised and self-supervised learning. *Magnetic Resonance in Medicine* **90**, 2052–2070 (2023).
74. L. C. Bell, E. Shimron, Sharing data is essential for the future of AI in medical imaging. *Radiology: Artificial Intelligence* **6**, e230337 (2023).
75. M. Lyu, L. Mei, S. Huang, S. Liu, Y. Li, K. Yang, Y. Liu, Y. Dong, L. Dong, E. X. Wu, M4Raw: A multi-contrast, multi-repetition, multi-channel MRI k-space dataset for low-field MRI research. *Scientific Data* **10**, 264 (2023).
76. A. E. Campbell-Washburn, R. Ramasawmy, M. C. Restivo, I. Bhattacharya, B. Basar, D. A. Herzka, M. S. Hansen, T. Rogers, W. Patricia Bandettini, D. R. McGuirt, C. Mancini, D. Grodzki, R. Schneider, W. Majeed, H. Bhat, H. Xue, J. Moss, A. A. Malayeri, E. C. Jones, A. P. Koretsky, P. Kellman, M. Y. Chen, R. J. Lederman, R. S. Balaban, Opportunities in interventional and diagnostic imaging by using high-performance low-field-strength MRI. *Radiology* **293**, 384-393 (2019).
77. P. J. Keall, C. Brighi, C. G. Hurst, G. Liney, P. Z. Y. Liu, S. Lydiard, C. Paganelli, T. Pham, S. Shan, A. C. Tree, U. A. van der Heide, D. E. J. Waddington, B. Whelan, Integrated MRI-guided radiotherapy — opportunities and challenges. *Nature Reviews Clinical Oncology* **19**, 458-470 (2022).
78. J. Grover, P. Z. Y. Liu, B. Dong, S. Shan, B. Whelan, P. Keall, D. E. J. Waddington, Super-resolution neural networks improve the spatiotemporal resolution of adaptive MRI-guided radiation therapy. *Communications Medicine* **4**, 64-64 (2024).
79. M. Uecker, P. Lai, M. J. Murphy, P. Virtue, M. Elad, J. M. Pauly, S. S. Vasanaawala, M. Lustig, ESPIRiT - An eigenvalue approach to autocalibrating parallel MRI: Where SENSE meets GRAPPA. *Magnetic Resonance in Medicine* **71**, 990-1001 (2014).
80. F. Ong, M. Lustig, SigPy: a python package for high performance iterative reconstruction. *27th Annual Meeting of the International Society of Magnetic Resonance in Medicine* (2019), p. 4819.

81. D. C. Van Essen, S. M. Smith, D. M. Barch, T. E. Behrens, E. Yacoub, K. Ugurbil, W.-M. H. Consortium, *et al.*, The WU-Minn human connectome project: an overview. *Neuroimage* **80**, 62–79 (2013).
82. N. Koonjoo, B. Primavera, J. P. Stockmann, T. Witzel, L. L. Wald, M. S. Rosen, Quadrature Head Coil for Brain Imaging at 6.5 mT. *25th Meeting of the International Society of Magnetic Resonance in Medicine* (2017), p. 2664.
83. T. Eo, H. Shin, Y. Jun, T. Kim, D. Hwang, Accelerating Cartesian MRI by domain-transform manifold learning in phase-encoding direction. *Medical Image Analysis* **63** (2020).
84. L. Sun, Z. Fan, X. Ding, Y. Huang, J. Paisley, Region-of-interest undersampled MRI reconstruction: A deep convolutional neural network approach. *Magnetic Resonance Imaging* **63**, 185-192 (2019).
85. J. Grover, D. E. J. Waddington, `lpips_torch2tf`. *Zenodo* p. <https://doi.org/10.5281/zenodo.12747631> (2024).
86. Z. Wang, Image Quality Assessment: From Error Visibility to Structural Similarity. *IEEE Transactions on Image Processing* **13**, 600-612 (2004).

Acknowledgements

General: The authors thank Nicholas Hindley and Helen Ball for providing valuable feedback on the complete draft of this manuscript.

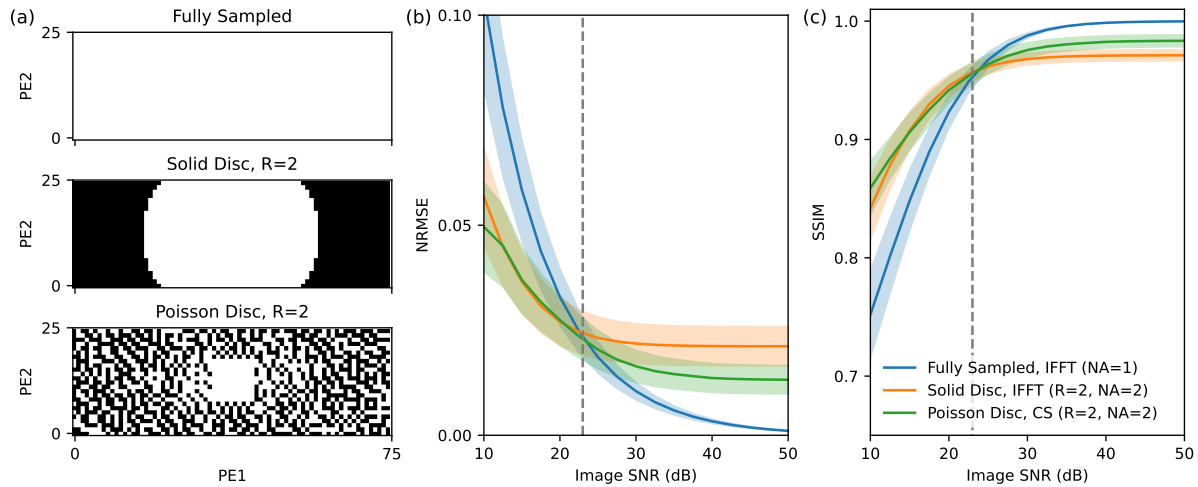
Funding: D.E.J.W. and T.B. received support from Australian National Health and Medical Research Council Investigator Grants 2017140 and 1194004, respectively. The information, data, or work presented herein was funded in part by the Advanced Research Projects Agency-Energy (ARPA-E), U.S. Department of Energy, under Award Number DE-AR0000823. The views and opinions of authors expressed herein do not necessarily state or reflect those of the United States Government or any agency thereof. M.S.R. acknowledges the gracious support of the Kiyomi and Ed Baird MGH Research Scholar Award. T.B. acknowledges the support of a Fulbright Future Scholarship, funded by The Kinghorn Foundation, from the Australian–American Fulbright Commission. E.S. is a Horev Fellow and acknowledges the generous support of the Technion’s Leaders in Science and Technology program, Zimin Foundation, and Alon Fellowship.

Author contributions: Conceptualization: DEJW, ES, and MSR. Methodology: SSha, NK, SShe, and JG. Investigation: SShe, TB, JK, AJS, and MSR. Visualization: DEJW, and ES. Funding acquisition: DEJW, ES, and MSR. Project administration: DEJW, and MSR. Supervision: DEJW, ES, and MSR. Writing – original draft: DEJW, and ES. Writing – review & editing: All.

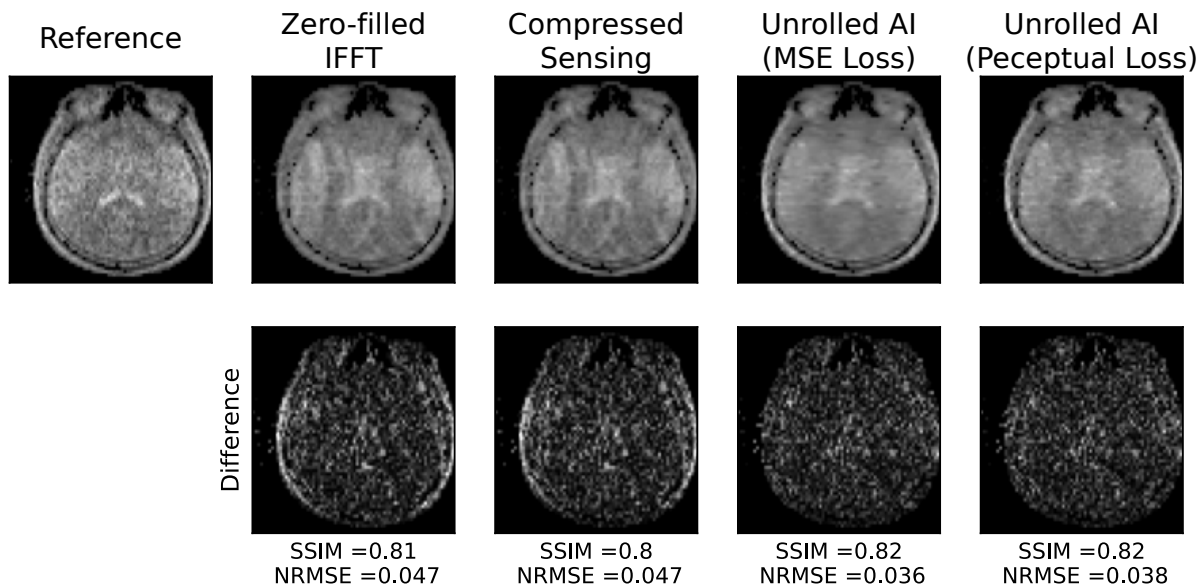
Data availability: The authors declare that the data supporting the findings of this study are available within the article and its supplementary information. Code necessary to reproduce the results of this paper has been made available at https://github.com/Image-X-Institute/Low_Field_MRI_Recon. Raw data are available from the corresponding author upon reasonable request.

Competing Interests: M.S.R. is a founder and equity holder of Hyperfine Inc. MSR is an equity holder of DeepSpin, GmbH. MSR holds a patent relating to the AUTOMAP method used in this work (11,620,772).

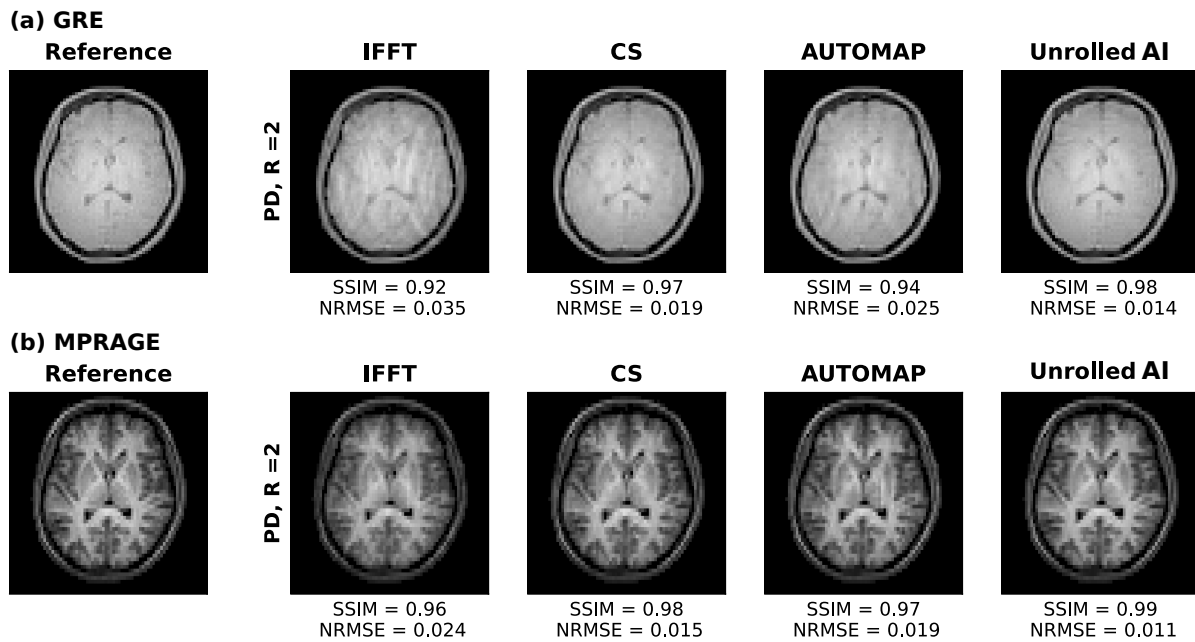
Supplementary Figures



Supplementary Figure 1: **Comparing accuracy of image reconstruction methods across different signal-to-noise ratios, for three sampling schemes.** (a) Fully-sampled acquisitions (NEX = 1) were compared to time-equivalent undersampled approaches ($R = 2$, NEX = 2) using a solid disc pattern and Poisson-disc-like pattern that fills the corners of k -space. (b) The accuracy of images reconstructed after different sampling approaches was evaluated on fastMRI data using normalized root-mean-square error (NRMSE) and structural similarity metrics (SSIM). Solid lines indicate the mean and shaded regions indicate the standard deviation across 100 brain volumes. The x -axis SNR values are calibrated to the Image SNR of the fully-sampled image (i.e. 20 dB is a linear Image SNR of 10, 40 dB is a linear Image SNR of 100).



Supplementary Figure 2: **Impact of loss functions on reconstruction quality** Fully-sampled data were acquired with a number of excitations (NEX) of 16. The NEX=16 data were retrospectively subsampled with an $R = 4$ Poisson disc mask and reconstructed with zero-filled Inverse Fast Fourier Transform (IFFT), Compressed Sensing, and unrolled AI techniques. During training, one unrolled AI method utilized Mean Square Error (MSE) loss and the other utilized LPIPS perceptual loss. Fully-sampled data were reconstructed with IFFT. Structural similarity (SSIM) error and normalized root-mean-square error (NRMSE) metrics were calculated relative to volumes reconstructed with IFFT from both Fully-sampled acquisitions. The MSE-trained network reconstructs the brain volume with more smoothing and a lower NRMSE than the LPIPS-trained network. However, the LPIPS-trained network fully removes the aliasing artifacts from the $R = 4$ undersampling and leaves other high-frequency features intact, which may potentially be beneficial to clinical interpretation.



Supplementary Figure 3: **Further Testing of Reconstruction Methods with High-field Data.** Fully-sampled, *single-channel* data were acquired at 3 T using GRE (a) and MPRAGE (b) sequences. A Poisson Disc mask ($R = 2$) was retrospectively applied to the k -space data. Normalized root-mean-square error (NRMSE) and Structural similarity (SSIM) values are calculated with respect to the reference image. unrolled AI outperforms all other reconstruction techniques. Some aliasing artifacts are visible in the AUTOMAP reconstruction of GRE data, indicating that the data-driven model is not generalizing to this new test data.